Tuning the Structural Isomers of Phenylenediammonium Cations to Afford Efficient and Stable Perovskite Solar Cells and Modules

Cheng Liu

North China Electric Power University

Yi Yang

North China Electric Power University

Kasparas Rakstys

Kaunas University of Technology

Arup Mahata

Istituto Italiano di Tecnologia   https://orcid.org/0000-0002-4995-3326

Marius Franckevicius

Center for Physical Sciences and Technology

Edoardo Mosconi

Computational Laboratory for Hybrid/Organic Photovoltaics (CLHYO)

Raminta Skackauskaite

Kaunas University of Technology

Bin Ding

EPFL

Onovbaramwen Jennifer Usiobo

Luxembourg Institute of Science and Technology (LIST)

Jean-Nicolas Audinot

Luxembourg Institute of Science and Technology, Materials Research and Technology

Hiroyuki Kanda

EPFL

Simonas Driukas

Center of Physical Sciences and Technology

Gabriele Kavaliauskaite

Center of Physical Sciences and Technology

Vidmantas Gulbinas

Center for Physical Sciences and Technology

Marc Dessimoz

EPFL

Vytautas Getautis

Kaunas University of Technology

Filippo De Angelis

Computational Laboratory for Hybrid/Organic Photovoltaics (CLHYO)

Yong Ding

North China Electric Power University

SongYuan Dai

Hefei Institutes of Physical Science, Chinese Academy of Sciences   https://orcid.org/0000-0001-5710-9208

Paul Dyson

École Polytechnique Fédérale de Lausanne

Mohammad Khaja Nazeeruddin (✉ mdkhaja.nazeeruddin@epfl.ch)

École Polytechnique Fédérale de Lausanne   https://orcid.org/0000-0001-5955-4786

Article

Abstract

Organic halide salt passivation is considered to be an essential strategy to reduce defects in state-of-the-art perovskite solar cells (PSCs). This strategy, however, suffers from the inevitable formation of in-plane favored two-dimensional (2D) perovskite layers with impaired charge transport, especially under thermal conditions, impeding photovoltaic performance and device scale-up. To overcome this limitation, we studied the energy barrier of 2D perovskite formation from *ortho*-, *meta*- and *para*-isomers of (phenylene)di(ethylammonium) iodide (PDEAI$_2$) that were designed for tailored defect passivation. Treatment with the most sterically hindered *ortho*-isomer not only prevents the formation of surficial 2D perovskite film, even at elevated temperatures, but also maximizes the passivation effect on both shallow- and deep-level defects. The ensuing PSCs achieve an efficiency of 23.9% with long-term operational stability (over 1000 hours). Importantly, a record efficiency of 21.4% for the perovskite module with an active area of 26 cm^2 was achieved.

1. Introduction

As the front runner among emerging photovoltaic technologies, perovskite solar cells (PSCs) with certified power conversion efficiencies (PCEs) over 25% show great promise for scale-up and future commercialization due to relatively simple and low-cost solution processes[1–4]. However, the disordered stoichiometric compositions at surfaces, the loss of organic components during thermal annealing, and the heterogeneous polycrystalline nature inevitably generate abundant defects in the solution-processed perovskite films, particularly at surfaces and grain boundaries[5–8]. Such defects incur electronic states in the bandgap of the perovskite and behave as nonradiative recombination centers, which shorten the carrier lifetime and limit the photovoltaic performance[9]. Moreover, these defects are responsible for local charge accumulation, accelerated ion migration, and the initial invasion of moisture or oxygen, ultimately causing device instability issues[3]. The defects also hinder the scale-up of PSCs to modules, thus restricting commercialization[10].

To address this problem, various defect reduction methods have been proposed including: i) composition tuning[11–13], ii) crystal growth regulation[14–16], and iii) surface passivation[17–20]. To date, surficial post-treatment by alkylammonium halides is commonly exploited to achieve efficient and stable perovskite devices, and many compounds have been evaluated[21–24]. Typically, an additional two-dimensional (2D) perovskite layer is formed on top of the primary perovskite absorber after treatment with alkylammonium halides, improving the stability of the devices[8,25,26]. A stubborn in-plane orientation is usually obtained for the surficial 2D perovskite layer, which potentially suppresses charge transport and draws back the passivation effect, especially when using bulkier spacer cations[27–29]. For this reason, recently, You et al. removed the annealing process after post-treatment to enable a thin phenylethylammonium iodide (PEAI) layer instead of a 2D perovskite layer for more effective surface passivation[30]. As a result, they achieved a certified PCE of over 23%, benefiting from a combination of promotion of charge transport by the π-conjugated phenyl rings, reduction of Pb^{2+} interstitials through amine coordination, and filling of iodine

vacancies by iodide ions[17]. However, these devices still suffered from a plummet in PCE under higher operating temperatures due to the conversion of PEAI to 2D PEA_2PbI_4. Therefore, an alkylammonium halide that can sustain higher temperatures without undergoing 2D perovskite formation is highly desirable to effectively passivate surface defects for efficient and stable PSCs and modules.

Herein, we describe surface passivation of perovskite films using *ortho*-(phenylene)di(ethylammonium) iodide (*o*-$PDEAI_2$) that leads to high-performance PSCs and modules. From an investigation of the *ortho*-, *meta*-, and *para*-isomers for $PDEAI_2$, the *ortho*-isomer effectively increases the energy barrier of the 2D perovskite formation and prevents the bulky organic cations from entering the perovskite lattice even at elevated temperatures. Surficial *o*-$PDEAI_2$ exhibits a comprehensive passivation effect on both shallow- and deep-level defects, which suppresses non-radiative recombination and improves interfacial charge extraction, resulting in a PCE of 23.9% in PSCs with enhanced long-term stability at ambient and elevated temperatures, and light-soaking conditions. Furthermore, a *o*-$PDEAI_2$-based perovskite module, with an active area of 26 cm^2, presents a record efficiency of 21.4%.

2. Results And Discussion

Isomer construction for suppressing 2D perovskite formation

The *ortho*-, *meta*-, and *para*-isomers of $PDEAI_2$ (Fig. 1a) were prepared and further details are provided in the Supplementary Information. To examine their potential to form 2D perovskites, films composed of equimolar quantities of $PDEAI_2$ and PbI_2 were fabricated. The X-ray diffraction (XRD) patterns of the *para*-$PDEAI_2$ (*p*-$PDEAI_2$)-based film (Fig. 1b) exhibits a dominant peak at ~7.15° associated with (002) lattice reflections of the 2D (*p*-PDEA)PbI_4 perovskite[31,32]. The *meta*-$PDEAI_2$ (*m*-$PDEAI_2$)-based film contains the same peak, but with a much lower relative intensity, implying that the 2D perovskite is formed, but to a much lower extent. The non-perovskite amorphous XRD pattern observed in the *o*-$PDEAI_2$-based film suggests that the 2D perovskite cannot be formed. Absorption and photoluminescence (PL) spectra reveal a similar trend (Fig. 1c). The *p*-$PDEAI_2$-based film shows an exciton absorption around 516 nm and a PL emission around 532 nm, assigned to the characteristic peaks of 2D perovskite with layer thickness n = 1[33]. These optical characteristics were not observed in the *m*-$PDEAI_2$-based sample due to the negligible 2D component in the film. Similarly, no absorption or emission signal was identified in the region 500−600 nm for *o*-$PDEAI_2$-based film, indicating that the formation of 2D perovskite is disfavored.

Next, $PDEAI_2$ isopropanol solutions were spin-coated onto the perovskite surface and experiments were performed to determine whether the surficial 2D perovskite is formed during the post-treatment process, especially under thermal induction. Widely used PEAI was employed for comparison. Figure 1d displays the temperature-dependent PL spectra of perovskite films under 450 nm excitation. As the temperature increases, the films deposited with PEAI and *p*-$PDEAI_2$ show enhanced emission in the 510−540 nm region, evidencing the growth of 2D perovskite with n = 1 on the film surface (Fig. 1b). In contrast, post-

treatment with m-PDEAI$_2$ and o-PDEAI$_2$ did not lead to the formation of surficial 2D perovskite, even at elevated temperatures. This was further confirmed by the temperature-dependent XRD (Fig. 1e and Supplementary Fig. 1), where reinforced (002) reflections of 2D perovskite were observed for the p-PDEAI$_2$- and PEAI-treated films whereas no peak was observed for the other two films. The upper 2D (p-PDEA)PbI$_4$ perovskite shows a lower diffraction intensity than that of the (PEA)$_2$PbI$_4$, which is commonly observed for other Dion-Jacobson (DJ) perovskites[31,34]. Grazing-incidence wide-angle X-ray scattering (GIWAXS) was used to probe the crystal orientation of the annealed films (Fig. 1f). The surficial (PEA)$_2$PbI$_4$ exhibits a combined feature of diffraction arcs and Bragg spots along the q_z direction at 0.39 Å^{-1} and 0.78 Å^{-1}, implying a random but predominantly in-plane orientation of the (002) and (004) crystal planes. A similar orientation was observed for (p-PDEA)PbI$_4$ with the characteristic (002) crystal plane at q_z = 0.51 Å^{-1}. Only diffraction signals corresponding to the three-dimensional (3D) perovskite (q_z = 1.00 Å^{-1}) and excess PbI$_2$ (q_z = 0.91 Å^{-1}) were identified for the m-PDEAI$_2$- and o-PDEAI$_2$-treated films, which is consistent with the XRD results (Supplementary Fig. 1). It is evident that both the monoammonium and the $para$-diammonium substituents on the phenyl ring enable organic halide salts to react with PbI$_2$ from the underlying 3D perovskite during the post-treatment process and form an in-plane-orientation dominated 2D perovskite on the surface (Fig. 1g). The arbitrary, especially in-plane, orientation will block the charge transport along with the inorganic framework due to the alternant insulating organic layers[35]. In contrast, m-PDEAI$_2$ and o-PDEAI$_2$ form a thin organic halide salt layer instead of 2D perovskite layer on the surface, which may avoid the energy disorder and the efficiency loss at elevated operating temperatures.

Density functional theory (DFT) calculations were used to understand the specific behavior of each PDEAI$_2$ isomer. The formation energies of 2D perovskites formed from p-PDEAI$_2$, m-PDEAI$_2$ or o-PDEAI$_2$ were calculated (Fig. 2a and Supplementary Table 1). The formation of 2D perovskite with p-PDEAI$_2$ and m-PDEAI$_2$ are energetically more favorable than o-PDEAI$_2$. We further checked the possibility of the formation 2D perovskite with a larger layer thickness and calculated the reaction thermodynamics of the process with the different isomers. Supplementary Fig. 2 and Supplementary Table 1 indicate that the reactions of p-PDEAI$_2$ and m-PDEAI$_2$ processes are more favorable than that of o-PDEAI$_2$. This difference is due to the suitable matching between the distance of two -CH$_2$-CH$_2$-NH$_3{}^+$ groups of the cations and the distance of adjacent octahedral voids on the perovskite. As can be seen in Supplementary Fig. 3, the lowest mismatching distances are 0.85, 0.15 and 1.85 Å for p-PDEAI$_2$, m-PDEAI$_2$ and o-PDEAI$_2$, respectively. The formation of quasi-2D perovskite is also likely to be energetically costly for the o-PDEAI$_2$, which is nicely reflected by the reaction energy values (Supplementary Table 1). Thus, the model demonstrates that o-PDEAI$_2$ possesses the highest formation energy barrier of surficial 2D perovskite among the PDEAI$_2$ isomers, in good agreement with the experimental observations.

Passivation effects on photovoltaic performance

In order to investigate the surface passivation effect, adsorption energies were calculated by depositing the p-PDEAI$_2$, m-PDEAI$_2$ and o-PDEAI$_2$ on the perovskite surface considering both the ethyl ammonium and phenyl ring adsorption modes (Fig. 2b and Supplementary Table 2). The calculations indicate that all three cations show similar surface passivation if only adsorption of one molecule is considered. However, passivation is achieved by the cumulative effect related to the number of cations that can be adsorbed per unit surface area. The optimized structures were processed to estimate the maximum number of cations that may be adsorbed on a 2 × 2 supercell (17.7 Å^2) of perovskite surface, as illustrated in the insets of Fig. 2b. For p-PDEAI$_2$ only 4 cations can be adsorbed, increasing to 4−6 for m-PDEAI$_2$ and 6 for o-PDEAI$_2$. Therefore, it can be qualitatively argued that o-PDEAI$_2$ shows a better surface passivation effect due to higher coverage which may reduce the probability of defect formation.

To examine the passivation effect, we incorporated the PDEAI$_2$ isomers onto the perovskite film with a surficial morphology corresponding to that shown in Supplementary Fig. 4, and the photovoltaic devices were fabricated with a typical configuration consisting of fluorine-doped tin oxide (FTO)/TiO$_2$/SnO$_2$/perovskite/PDEAI$_2$/2,2',7,7'-tetrakis-(N,N-di-4-methoxyphenylamino)-9,9'spirobifluorene (spiro-OMeTAD)/Au (Fig. 3a). Current density (J)-voltage (V) characteristics of the devices are compared in Supplementary Fig. 5a and Supplementary Table 3. As expected, the devices with p-PDEAI$_2$ show slightly lower PCEs compared to the control devices, ascribed to the disordered 2D (p-PDEA)PbI$_4$ layer that hinders vertical charge transport. Interestingly, a comparatively low efficiency was observed for the m-PDEAI$_2$-based devices. This may be rationalized by the two -CH$_2$-CH$_2$-NH$_3^+$ groups of m-PDEA anchoring at adjacent octahedral voids of the perovskite surface (Supplementary Fig. 3), which might cause carrier stagnation and resultant charge recombination. Among the three isomers, o-PDEAI$_2$ has the best passivation effect, improving the average PCE from 20.88% of the control device to 22.41%, mainly reflected by the enhanced fill factor (FF) and open-circuit voltage (V_{OC}). The effective passivation of o-PDEAI$_2$ may be attributed to (i) the high adsorption density on the perovskite, (ii) the strong adsorption energy due to the diammonium structure, and (iii) the electrostatic interactions with the defective perovskite surface[17,36]. As a result, the best-performing PSC passivated with o-PDEAI$_2$ shows a PCE of 23.92%, with a V_{OC} of 1.157 V, a short-circuit current (J_{SC}) of 24.75 mA cm^{-2}, and an FF of 83.50%, compared to the best control device with a PCE of 21.94%, V_{OC} of 1.135 V, J_{SC} of 24.49 mA cm^{-2} and FF of 79.00%. The integrated J_{SC} values from the external quantum efficiency (EQE) spectra in Supplementary Fig. 5b matches well with those measured from the J-V curves (< 1% discrepancy). A stabilized power output of 23.50% and negligible hysteresis are demonstrated for the o-PDEAI$_2$-based device as shown in Fig. 3b. Also, the statistic histogram reveals good reproductivity with 75% of the devices having PCEs exceeding 22% (Fig. 3c), confirming the effectiveness of o-PDEAI$_2$ passivation.

To elucidate the passivation effect on the hole extraction and carrier dynamics in the devices, voltage-dependent transient PL and transient photocurrent studies were performed. Supplementary Fig. 6a-e shows the PL decay kinetics obtained for different devices at various applied voltages. All devices show bicomponential PL decay, and the dependences of the average decay times on the applied voltage are

shown in Fig. 3d. The applied voltage reduces the average decay times, indicating that they are at least partly determined by the carrier extraction. The average decay times anticorrelate with the device efficiency and particularly with FFs, where the devices with faster PL decays show better performance. Specifically, o-PDEAl$_2$ passivation causes the fastest PL decay attributed to the improved hole extraction, whereas the m-PDEAl$_2$ passivated film shows much slower PL decay, which indicates impaired hole extraction deteriorating the device performance[37].

To exclude the influence of the built-in electric field present in solar cells, we have additionally investigated the PL decays in the treated with PDEAl$_2$ and nontreated perovskite films covered with spiro-OMeTAD deposited on glass substrates (see Supplementary Fig. 6f for kinetics and Supplementary Table 4 for bi-exponential fitting parameters). For comparison, we have also investigated a pure nontreated perovskite film, which showed a long lifetime of 284 ns indicating a high material quality[38]. The spiro-OMeTAD layer significantly shortens the PL decay due to efficient hole extraction. Passivation with the different PDEAl$_2$ isomers shows qualitatively similar results as for the complete devices confirming their influence on the hole extraction rate.

The carrier extraction dynamics were revealed by transient photocurrent measurements. Due to the high capacitance of the devices restricting the time resolution of photocurrent measurements, the carrier extraction investigations were performed in integral mode measuring discharging of the device capacitance by photocurrents, when voltage was applied through a high (1 kΩ) resistor. The signal growth, in this case, corresponds to the cumulated extracted charge. Figure 3e shows the normalized charge extraction kinetics under an applied voltage of 1 V. The o-PDEAl$_2$-passivated device shows the fastest carrier extraction of < 0.2 µs. (The partial signal drop during about 0.4-2.0 µs is caused by the sample recharging by the capacitance from the external circuit.) The control device shows similarly fast initial extraction, however, an additional slow extraction component is also observed. Significantly slower charge extraction from the m-PDEAl$_2$-treated device is in good agreement with the PL decay data.

We further addressed the role of PDEAl$_2$ passivation by investigating transient photocurrent kinetics in lateral sample geometry. The perovskite films were formed on an interdigitated comb of Pt electrodes (IDE) with 5 µm interelectrode distances and a spiro-MeOTAD layer was deposited on top of perovskite films. Due to the large, 5 µm interelectrode distance, the carrier extraction was slow. We also used low excitation intensity, when carrier recombination could be ignored. In these conditions, the photocurrent kinetics on a sub-microsecond time scale was mainly determined by the carrier trapping and by the hole extraction to hole transport layer (HTL)[39]. The control device with HTL shows faster photocurrent decay than that without HTL during initial ~ 50 ns due to the hole extraction (Fig. 3f). The influence of PDEAl$_2$ treatment is expected to be bilateral: passivation of surface traps shall cause slower photocurrent decay, and modification of the hole extraction rate may cause additional photocurrent changes. Indeed, all passivated samples show slower photocurrent decay indicating reduced carrier trapping. The m-PDEAl$_2$-treated sample shows particularly slow decay, apparently because of reduced carrier trapping and the prevented hole extraction. While the o-PDEAl$_2$-treated sample shows similar slow carrier decay during

initial ~ 20 ns, due to reduced carrier trapping, but at longer times the photocurrent decays faster attributed to the improved hole extraction. The overall transient PL and photocurrent results provide indications of interfacial trap passivation by the PDEAI$_2$ isomers and also demonstrate that o-PDEAI$_2$ treatment reduces the carrier transfer barrier at the perovskite/HTL junction and effectively increases the hole extraction rate contributing to the FF enhancement of PSCs.

Ultraviolet photoelectron spectroscopy (UPS) was used to understand the surface energy band structure with and without o-PDEAI$_2$. The work function is determined to be -4.45 eV and − 4.91 eV for the pristine perovskite surface and the o-PDEAI$_2$ passivated surface, respectively (Supplementary Fig. 7). This shift is in accordance with the change in surface potential probed by Kelvin probe force microscopy (KPFM) as reflected in Fig. 4a. The o-PDEAI$_2$-passivated surface exhibits a lower average electronic chemical potential (0.16 mV) than that of the control (0.33 mV). The downshift suggests a more p-type surface after o-PDEAI$_2$ treatment, which can improve hole extraction and cause band-bending for higher V_{OC} values[40]. Confocal PL microscopy mapping was applied to probe the homogeneity of perovskite films. The film with o-PDEAI$_2$ presents more uniform PL emission compared to the control film, indicating less surface defect densities (Fig. 4b). This is also revealed by the cathodoluminescence (CL) intensity maps, where a more homogeneous distribution was demonstrated for the film with o-PDEAI$_2$ passivation (Fig. 4c). To complement these data the corresponding CL spectra (Supplementary Fig. 8) confirm that o-PDEAI$_2$ treatment does not induce 2D perovskite formation on the surface and the CL peaks at around 508 nm may be assigned to the presence of excess PbI$_2$ in both films. To confirm the presence of o-PDEAI$_2$ on the perovskite surface, X-ray photoelectron spectroscopy (XPS) was performed. The high-resolution XPS patterns of C1s (Supplementary Fig. 9) show an emerging peak at ~ 291.0 eV, corresponding to the conjugated π-π bonding of the phenyl group in o-PDEAI$_2$[30]. The XPS pattern of Pb 4f for the control film displays two dominant peaks located at 138. 8 and 143.7 eV, assigned to the Pb 4f$_{7/2}$ and Pb 4f$_{5/2}$, respectively (Fig. 4d), which shift to 139.1 and 144.0 eV for the film with o-PDEAI$_2$. This shift to higher binding energies reflects the modified electronic states of the perovskite atoms due to interactions between o-PDEAI$_2$ and the perovskite surface[41]. In addition, another two peaks located at 137.0 and 141.9 eV arising from the metallic Pb were observed in the control film, which were not observed in the passivated film. This implies that o-PDEAI$_2$ can combine with under-coordinated Pb^{2+} ions and thereby avoid the formation of metallic Pb, thus restraining the ionic defects and improving the operational stability of the PSCs[42]. To quantify the passivation effect of o-PDEAI$_2$, a Mott-Schottky analysis and trap density of states (tDOS) measurements were conducted on the complete devices. As indicated in Fig. 4e, the higher built-in potential (1.146 vs 1.121 V) and lower interfacial charge density (2.73×10^{15} vs 3.50×10^{15} cm^{-3}) for the o-PDEAI$_2$-passivated device demonstrates that the o-PDEAI$_2$ layer can enhance the driving force of carrier injection and reduce the recombination losses at the interface.[10] The tDOS distribution under each energy demarcation was characterized as shown in Fig. 4f. The charging and discharging of trap states within the bandgap contributes to a larger variation in capacitance with the change of frequencies. Thus, the frequency differential capacitance can disclose

the defects at certain energy demarcations[43]. It was found that the control device has higher trap densities of 10^{19}-10^{21} m^{-3} eV^{-1} over three trap bands. After o-PDEAI$_2$ treatment, the tDOS was reduced over the entire energy region, to 10^{18}-10^{20} m^{-3} eV^{-1}, confirming that the o-PDEAI$_2$ effectively passivate the defects with both shallow and deep energy levels on the surface of perovskite film.

We further evaluated the scalability of surface passivation by o-PDEAI$_2$ by fabricating a perovskite solar module with a total active area of 26.00 cm^2. (Fig. 5a). The module was completed by laser etching with 9 subcells in series and the interconnection is schematically illustrated in Fig. 5b. Encouragingly, the perovskite solar module based on o-PDEAI$_2$ passivation exhibits a PCE of 21.36%, with a V_{OC} of 10.30 V, a J_{SC} of 2.71 mA cm^{-2} and an FF of 76.40% (Fig. 5c and Supplementary Fig. 10), which is the highest efficiency reported so far for perovskite solar modules on the active area (Supplementary Table 5)[44]. The high module performance originates from the good uniformity of the perovskite layer, the reduced trap density, and suppressed interfacial recombination, confirming the utility of the o-PDEAI$_2$ passivation strategy for scale-up of PSCs.

Shelf life and operational stability

Long-term stability tests were carried out to study the influence of o-PDEAI$_2$ layer on device stability. The PCEs of the unencapsulated devices under a RH of 40−50% were first tracked over time (Fig. 5d). The control device maintains 58% of the initial PCE (20.82%) after 1008 hours, compared to that of 85% for the o-PDEAI$_2$ passivated device with an initial efficiency of 22.65%. The thermal stability was also evaluated by heating the perovskite films and corresponding devices at 85°C in a nitrogen atmosphere. As shown in Fig. 5e, the o-PDEAI$_2$ passivated device (initial PCE 22.38%) degrades by 25% over 1000 hours, compared to a 49% decrease for the control device (initial PCE 20.32%). Interestingly, an efficiency plummet is not observed at the start of the annealing process. That is, the suppression of converting o-PDEAI$_2$ into 2D perovskite effectively retains the passivation effect under constant heating, and avoids the PCE drop at the initial stage, which was normally observed in the widely used PEAI passivation[30]. XRD tracking shows that the thermal degradation of these perovskite films results from the decomposition of the perovskite material (Fig. 5f). The control film shows an increase in the intensity of the peaks that correspond to PbI$_2$, whereas decomposition is retarded after o-PDEAI$_2$ passivation, indicating the o-PDEAI$_2$ passivation layer reduces the release of volatile organic components and enhances the resistance to heat of the perovskite material[45]. The continuous performance of the unencapsulated PSCs was also examined by MPPT under 1 sun illumination in an inert atmosphere. The device passivated with o-PDEAI$_2$ exhibits enhanced light stability, maintaining > 90% of its original PCE after 1100 h, outperforming the control device, which degrades to > 60% of the initial PCE. The robust ambient and operational stability of the o-PDEAI$_2$-based device may be attributed to the hydrophobicity of the phenyl group, the mitigated interfacial charge accumulation, and the suppressed ion migration benefiting from the passivation of defects[46,47].

3. Conclusions

We demonstrate that o-PDEAI$_2$ is an effective passivation agent which affords highly efficient and stable PSCs. Experimental and theoretical studies indicate that locating the two ammonium cations in the most sterically hindered *ortho* position endows o-PDEAI$_2$ with an energy barrier for the formation of the in-plane favored 2D perovskite together with stronger defect passivation effects compared to the other structural isomers, to significantly reduce interfacial charge recombination. Passivation with o-PDEAI$_2$ boosts the efficiency of PSCs and modules (26 cm^2) to 23.9% and 21.4%, respectively, while ensuring long-term stabilities over 1000 h. This work should pave the way for scaling up perovskite photovoltaics to sizes of commercial relevance.

Methods

Device Fabrication. The TiO$_2$ compact layer was deposited onto cleaned FTO (Nippon Sheet Glass, TEC8) substrates by spray pyrolysis of titanium diisopropoxide bis(acetylacetonate) (75 wt. % in isopropanol, Sigma-Aldrich) diluted in anhydrous isopropanol (99.8%, Acros Organics) with 1:20 volume ratio at 450°C and then annealed at 450°C for 30 min. TiO$_2$ paste (30NR-D, GreatCell Solar) was diluted in anhydrous ethanol (99.8%, Acros Organics) with a weight ratio of 1:10 and spin-coated onto substrates at 3000 rpm for 20 s. The films were then annealed at 500°C for 30 min in air. After cooling, 0.1 M SnCl$_4$ (99%, Acros Organics) aqueous solution was deposited on substrates at 3000 rpm for 30 s. The films were then dried at 190°C for 1 h and transferred into a nitrogen glovebox. 1.45 M perovskite precursors (PbI$_2$: PbBr$_2$: FAI: MAI: CsI: MACl = 0.98: 0.02: 0.81: 0.04: 0.05: 0.20) were dissolved in the mixed DMF (99.8%, Acros Organics): DMSO (99.7%, Acros Organics) = 4:1 (volume ratio) solvent. The perovskite solution was spin-coated on substrates at 1000 rpm for 12 s and 5000 rpm for 28 s, respectively. 200 μL of chlorobenzene (99.8%, Acros Organics) was dropped onto the spinning films at 15 s of the second step, followed by annealing at 100°C for 10 min and 150°C for 10 min. For the post treatment, phenyldiethylammonium iodide (PDEAI$_2$) solutions with a concentration of 2 mg mL^{-1} in anhydrous isopropanol (99.8%, Acros Organics) were deposited on perovskite films at 4000 rpm for 20s, followed by annealing at 100 for 5 min. 0.06 M spiro-OMeTAD was dissolved in chlorobenzene (99.8%, Acros Organics), adding 0.2 M 4-*tert*-Butylpyridine (98%, Sigma-Aldrich), 0.03 M bis(trifluoromethanesulfonyl)-imide lithium (LiTFSI, 99.0%, Sigma-Aldrich) in acetonitrile (99.9%, Acros Organics) and 0.0035 M FK209 Co(III) TFSI (GreatCell Solar) in acetonitrile (99.9%, Acros Organics). The spiro-OMeTAD solution was spin-coated at 3000 rpm for 20 s, followed by thermal evaporation of a 70 nm gold electrode under high vacuum. For module fabrication, 6.5 cm × 7 cm FTO substrates were patterned by laser with nine sub-cells connected in series. The film deposition processes were the same as the normal solar cells as described above. The geometric fill factor (GFF) was calculated to be 90.2%, which was defined as the active area divided by the designated area.

Characterization. The GIWAXS was measured with a photon energy of 8.03 keV (1.55 Å) at an incident angle of 0.3°. PL decay kinetics were measured using the Edinburgh Instruments time correlated single

photon counting (TCSPC) fluorescence spectrometer F900. The KPFM images were acquired using an MFP-3D Infinity with AC bias modulation at 7.5KHz and 4V amplitude in ambient. The UPS was measured by an AXIS Nova spectrometer (Kratos Analytical Ltd, UK) with a He-I source (21.22 eV). The XPS was examined by VersaProbe II (Physical Electronics Inc.) with an Al-Ka source of 1486.6 eV. The micro-PL maps were obtained with an Acton Standard Series SP-2558 laser confocal Raman spectrometer (Princeton Instruments), a digital CCD (PIXIS:100B_eXcelon) and a 485 nm laser (PicoQuant LDH-P-C-485). Cathodoluminescence (CL) measurements were performed on the Attolight ROSA 4634 CL SEM at 1kV and 50 nm per pixel for the image of 128×128 pixel.

Current density (J)-voltage (V) characteristics of the devices were characterized by a commercial solar simulator (Oriel, 450 W xenon, AAA class) combined with a Keithley 2400 source meter at room temperature in air. The light intensity was calibrated before each measurement with a Si reference cell (KG5, Newport) to match with the AM 1.5G (100 mW cm^{-2}) standard. The voltage scan rate and scan step were 125 mV s^{-1} and 10 mV, respectively. No light soaking or voltage bias was applied before the measurement and the active area of the cells was defined by a black metal mask with square aperture of the area of 0.09 cm^2. For solar modules, the voltage scan rate was 5 V s^{-1} and scan steps was 50 mV, and the active area of modules was defined by an opaque metal mask with 9 individual rectangular apertures of the total area of 26 cm^2. The external quantum efficiency (EQE) spectra were recorded with an IQE200B (Oriel). The stability test was conducted under 100 mW cm^{-2} LED illumination at 25°C and the devices were sealed in a cell holder flushed with a N_2 flow of ~ 30 mL/min. For the humidity test, the unsealed solar cells were kept in the ambient of 40−50% relative humidity (RH) monitored by a hygrometer at room temperature in the dark. For the thermal stability test, the solar cells were kept at 85 °C in nitrogen under dark conditions. Transient photocurrent measurements were performed with an Agilent Technologies DS05054A oscilloscope using 1kΩ input resistor and a Tektronix AFG 3101 function generator. The Mott-Schottky curve was recorded with an SP-200 potentiostat (BioLogic).

Declarations

Acknowledgements

Author Contributions

Competing Interests statement

The authors declare no competing financial interests.

References

1   Yoo, J. J. *et al.* Efficient perovskite solar cells via improved carrier management. *Nature* **590**, 587-593 (2021).

2   Jeong, J. *et al.* Pseudo-halide anion engineering for α-FAPbI$_3$ perovskite solar cells. *Nature* **592**, 381-385 (2021).

3   Ball, J. M. & Petrozza, A. Defects in perovskite-halides and their effects in solar cells. *Nat. Energy* **1**, 1-13 (2016).

4   Akkerman, Q. A. *et al.* Strongly emissive perovskite nanocrystal inks for high-voltage solar cells. *Nat. Energy* **2**, 1-7 (2016).

5   Wang, F., Bai, S., Tress, W., Hagfeldt, A. & Gao, F. Defects engineering for high-performance perovskite solar cells. *npj Flex. Electron.* **2**, 1-14 (2018).

6   Vaynzof, Y. The future of perovskite photovoltaics—thermal evaporation or solution processing? *Adv. Energy Mater.* **10**, 2003073 (2020).

7   Kim, H. *et al.* Optimal interfacial engineering with different length of alkylammonium halide for efficient and stable perovskite solar cells. *Adv. Energy Mater.* **9**, 1902740 (2019).

8   Liang, L., Luo, H., Hu, J., Li, H. & Gao, P. Efficient Perovskite Solar Cells by Reducing Interface-Mediated Recombination: a Bulky Amine Approach. *Adv. Energy Mater.* **10**, 2000197 (2020).

9   Ono, L. K., Liu, S. & Qi, Y. Reducing detrimental defects for high-performance metal halide perovskite solar cells. *Angew. Chem. Int. Ed.* **59**, 6676-6698 (2020).

10   Du, M. *et al.* High-Pressure Nitrogen-Extraction and Effective Passivation to Attain Highest Large-Area Perovskite Solar Module Efficiency. *Adv. Mater.* **32**, 2004979 (2020).

11   Saliba, M. *et al.* Cesium-containing triple cation perovskite solar cells: improved stability, reproducibility and high efficiency. *Energy Environ. Sci.* **9**, 1989-1997 (2016).

12   Jacobsson, T. J. *et al.* Unreacted PbI_2 as a double-edged sword for enhancing the performance of perovskite solar cells. *J. Am. Chem. Soc.* **138**, 10331-10343 (2016).

13   Jiang, Q. *et al.* Planar-structure perovskite solar cells with efficiency beyond 21%. *Adv. Mater.* **29**, 1703852 (2017).

14   Lin, Y.-H. *et al.* A piperidinium salt stabilizes efficient metal-halide perovskite solar cells. *Science* **369**, 96-102 (2020).

15   Zuo, C. & Ding, L. Drop-Casting to Make Efficient Perovskite Solar Cells under High Humidity. *Angew. Chem. Int. Ed.* **133**, 11342-11346 (2021).

16   Zhou, X. *et al.* Highly Efficient and Stable GABr-Modified Ideal-Bandgap (1.35 eV) Sn/Pb Perovskite Solar Cells Achieve 20.63% Efficiency with a Record Small Voc Deficit of 0.33 V. *Adv. Mater.* **32**, 1908107 (2020).

17   Gao, F., Zhao, Y., Zhang, X. & You, J. Recent progresses on defect passivation toward efficient perovskite solar cells. *Adv. Energy Mater.* **10**, 1902650 (2020).

18   Wu, S. *et al.* 2D metal-organic framework for stable perovskite solar cells with minimized lead leakage. *Nat. Nanotechnol.* **15**, 934-940 (2020).

19   Wu, X. *et al.* Efficient perovskite solar cells via surface passivation by a multifunctional small organic ionic compound. *J. Mater. Chem. A* **8**, 8313-8322 (2020).

20   Wang, X. et al. Engineering fluorinated-cation containing inverted perovskite solar cells with an efficiency of >21% and improved stability towards humidity. *Nat. Commun.* **12**, 52 (2021).

21   Grancini, G. *et al.* One-Year stable perovskite solar cells by 2D/3D interface engineering. *Nat. Commun.* **8**, 1-8 (2017).

22   Zhao, T., Chueh, C.-C., Chen, Q., Rajagopal, A. & Jen, A. K.-Y. Defect passivation of organic–inorganic hybrid perovskites by diammonium iodide toward high-performance photovoltaic devices. *ACS Energy Lett.* **1**, 757-763 (2016).

23   Liu, G. *et al.* Passivation effect of halogenated benzylammonium as a second spacer cation for improved photovoltaic performance of quasi-2D perovskite solar cells. *J. Mater. Chem. A* **8**, 5900-5906 (2020).

24   Zhou, Q. *et al.* Fluoroaromatic Cation-Assisted Planar Junction Perovskite Solar Cells with Improved V_{OC} and Stability: The Role of Fluorination Position. *Sol. RRL* **4**, 2000107, (2020).

25   Rajagopal, A., Yao, K. & Jen, A. K. Y. Toward perovskite solar cell commercialization: a perspective and research roadmap based on interfacial engineering. *Adv. Mater.* **30**, 1800455 (2018).

26   Mahmud, M. A. *et al.* Origin of Efficiency and Stability Enhancement in High-Performing Mixed Dimensional 2D-3D Perovskite Solar Cells: A Review. *Adv. Funct. Mater.*, 2009164 (2021).

27   Ansari, F. *et al.* Passivation mechanism exploiting surface dipoles affords high-performance perovskite solar cells. *J. Am. Chem. Soc.* **142**, 11428-11433 (2020).

28   Pan, H., Zhao, X., Gong, X., Shen, Y. & Wang, M. Atomic-Scale tailoring of organic cation of layered Ruddlesden-Popper perovskite compounds. *J. Phys. Chem. Lett.* **10**, 1813-1819 (2019).

29   Yang, Y. *et al.* Universal approach toward high-efficiency two-dimensional perovskite solar cells via a vertical-rotation process. *Energy Environ. Sci.* **13**, 3093-3101, (2020).

30   Jiang, Q. *et al.* Surface passivation of perovskite film for efficient solar cells. *Nat. Photonics* **13**, 460-466 (2019).

31   Li, Y. *et al.* Bifunctional organic spacers for formamidinium-based hybrid Dion–Jacobson two-dimensional perovskite solar cells. *Nano Lett.* **19**, 150-157 (2018).

32   Cao, D. H., Stoumpos, C. C., Farha, O. K., Hupp, J. T. & Kanatzidis, M. G. 2D homologous perovskites as light-absorbing materials for solar cell applications. *J. Am. Chem. Soc.* **137**, 7843-7850 (2015).

33   Xu, Y., Wang, M., Lei, Y., Ci, Z. & Jin, Z. Crystallization kinetics in 2D perovskite solar cells. *Adv. Energy Mater.* **10**, 2002558 (2020).

34   Cohen, B.-E., Li, Y., Meng, Q. & Etgar, L. Dion–Jacobson Two-Dimensional Perovskite Solar Cells Based on Benzene Dimethanammonium Cation. *Nano Lett.* **19**, 2588-2597 (2019).

35   Yang, Y. *et al.* Defect Suppression in Oriented 2D Perovskite Solar Cells with Efficiency over 18% via Rerouting Crystallization Pathway. *Adv. Energy Mater.*, **11**, 2002966 (2020).

36   Zhuang, J. *et al.* Interfacial passivation for perovskite solar cells: the effects of the functional group in phenethylammonium iodide. *ACS Energy Lett.* **4**, 2913-2921 (2019).

37   Paek, S. *et al.* Molecular Design and Operational Stability: Toward Stable 3D/2D Perovskite Interlayers. *Adv. Sci.* **7**, 2001014 (2020).

38   Drigo, N. *et al.* Doped but stable: spirobisacridine hole transporting materials for hysteresis-free and stable perovskite solar cells. *J. Am. Chem. Soc.* **142**, 1792-1800 (2019).

39   Jasiūnas, R., Gegevičius, R., Franckevičius, M., Jašinskas, V. & Gulbinas, V. Energy Barriers Restrict Charge Carrier Motion in MAPI Perovskite Films. *Adv. Opt. Mater.* **8**, 2000036 (2020).

40   Kanda, H. *et al.* Band-bending induced passivation: high performance and stable perovskite solar cells using a perhydropoly (silazane) precursor. *Energy Environ. Sci.* **13**, 1222-1230 (2020).

41   Wang, R. *et al.* Constructive molecular configurations for surface-defect passivation of perovskite photovoltaics. *Science* **366**, 1509-1513 (2019).

42   Zhang, H., Nazeeruddin, M. K. & Choy, W. C. Perovskite photovoltaics: the significant role of ligands in film formation, passivation, and stability. *Adv. Mater.* **31**, 1805702 (2019).

43   Wang, Q. *et al.* Large fill-factor bilayer iodine perovskite solar cells fabricated by a low-temperature solution-process. *Energy Environ. Sci.* **7**, 2359-2365 (2014).

44   Vaynzof, Y. Long live the perovskite module. *Nat. Energy* **6**, 578-579 (2021).

45   Zhang, T. *et al.* Stable and efficient 3D-2D perovskite-perovskite planar heterojunction solar cell without organic hole transport layer. *Joule* **2**, 2706-2721 (2018).

46   Hou, Y. *et al.* A generic interface to reduce the efficiency-stability-cost gap of perovskite solar cells. *Science* **358**, 1192-1197 (2017).

47   Christians, J. A. *et al.* Tailored interfaces of unencapsulated perovskite solar cells for >1,000 hour operational stability. *Nat. Energy* **3**, 68-74 (2018).
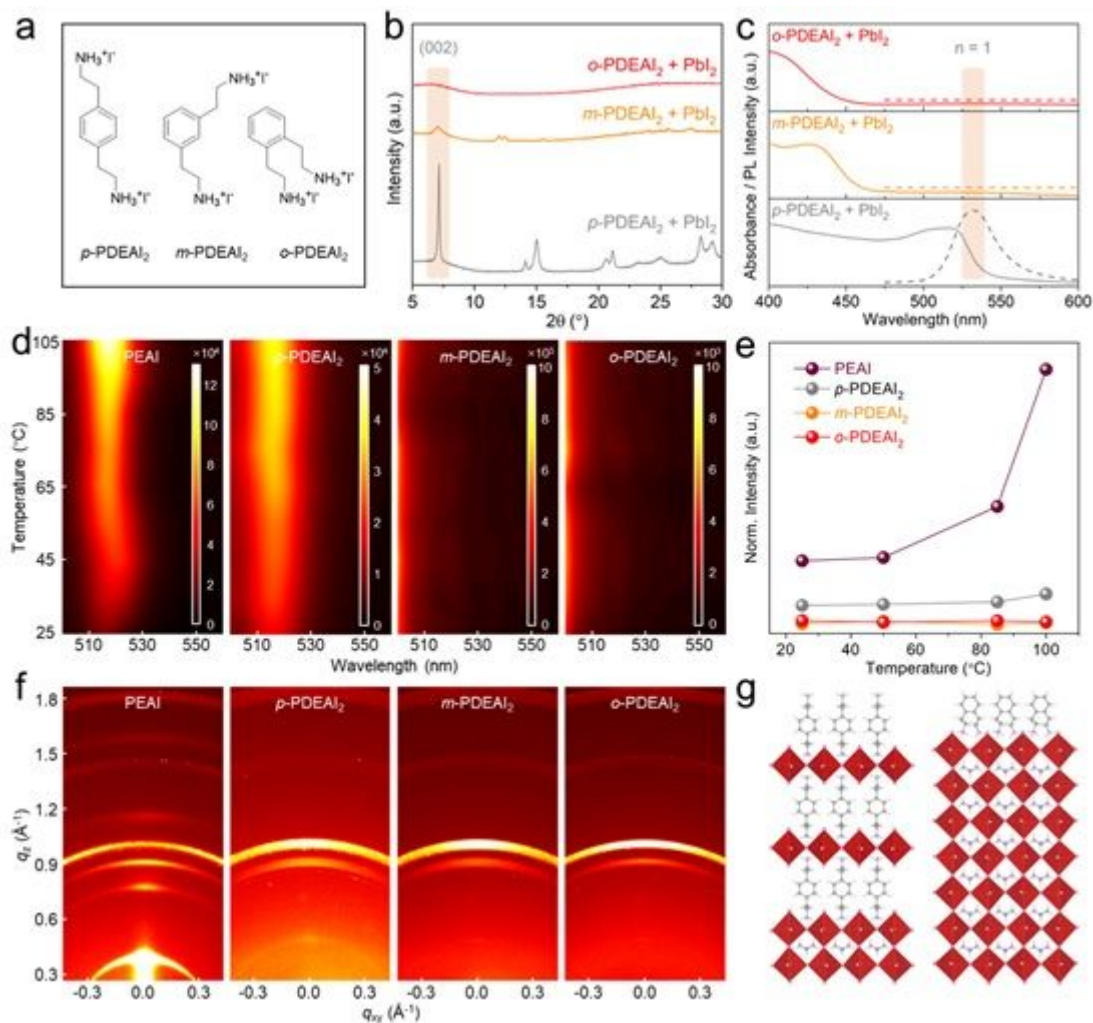
Figures

Figure 1

Structures of PDEAI2 and subsequent formation of 2D perovskites. a, The structures of the PDEAI2 isomers. b, XRD patterns of the films obtained from equimolar ratios of PDEAI2 and PbI2. c, Absorption and PL emission spectra of the films obtained from equimolar ratios of PDEAI2 and PbI2. d, Temperature-dependent PL images of the perovskite films treated with the different organic halide salts. e, Intensity of the (002) reflections of the surficial 2D perovskites as a function of annealing temperature for the post-treated perovskite films. f, GIWAXS images of the perovskite films following post-treatment. g, Schematic illustration of p-PDEAI2 and o-PDEAI2-assembled perovskite surface.
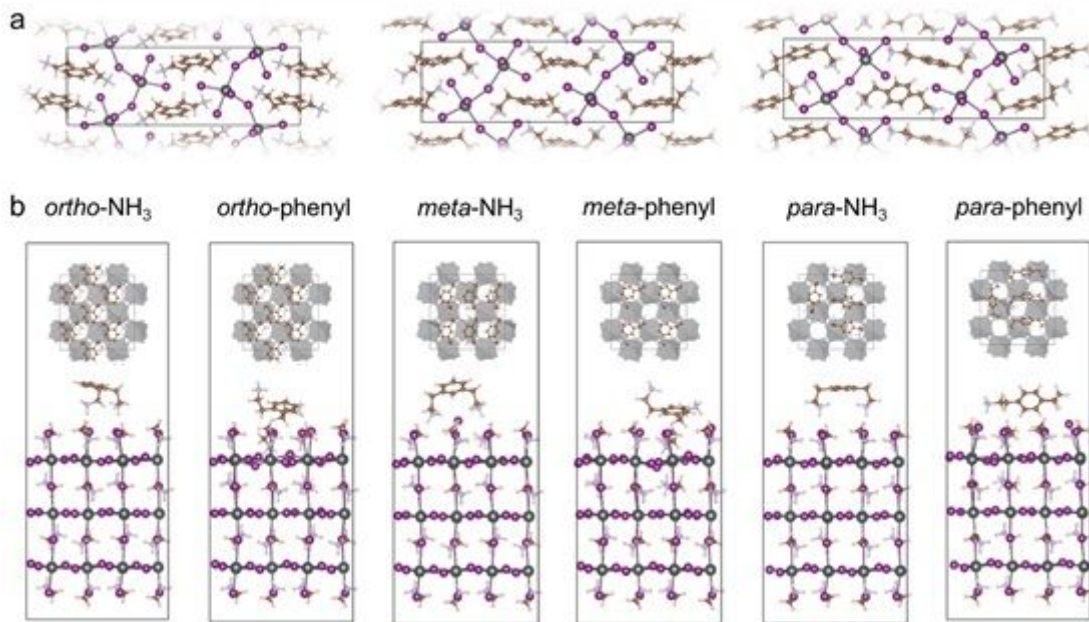
Figure 2

Theoretical modelling. a, Optimized 2D perovskites structures incorporating o-PDEAI2, m-PDEAI2 and p-PDEAI2. b, Optimized structures for the adsorption of 2D cations on the perovskite surface. The top insets indicate the maximum number of PDEA cations that can be adsorbed on a 2 × 2 perovskite surface. Schematic is based on the optimized coordinates of the corresponding structures and translating them in multiple numbers. For the o-PDEAI2 structures, both the modes adsorb in a similar manner.
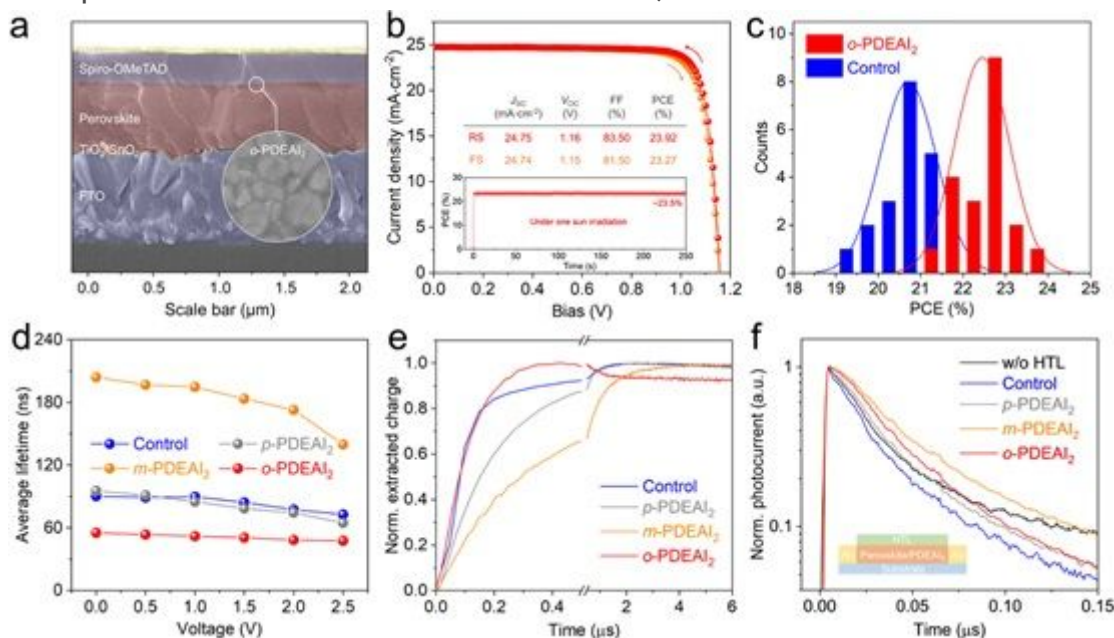

Figure 3

Passivation-layer-dependent device performance. a, The cross-sectional scanning electron microscope (SEM) image of the PSC passivated with o-PDEAI2. b, J-V characteristics of the champion device with o-PDEAI2 measured in both reverse (red) and forward (orange) scanning directions (the inset shows its

stabilized power output). c, The statistics of PCE distribution for devices with and without o-PDEAl2. (Statistics from 20 samples for each condition). The solid lines denote the Gauss distribution fitting for the PCE statistics. d, Voltage-dependent average PL lifetimes of the different devices. e, Integrated charge extraction curves of devices. f, Transient photocurrent decay in lateral sample geometry.
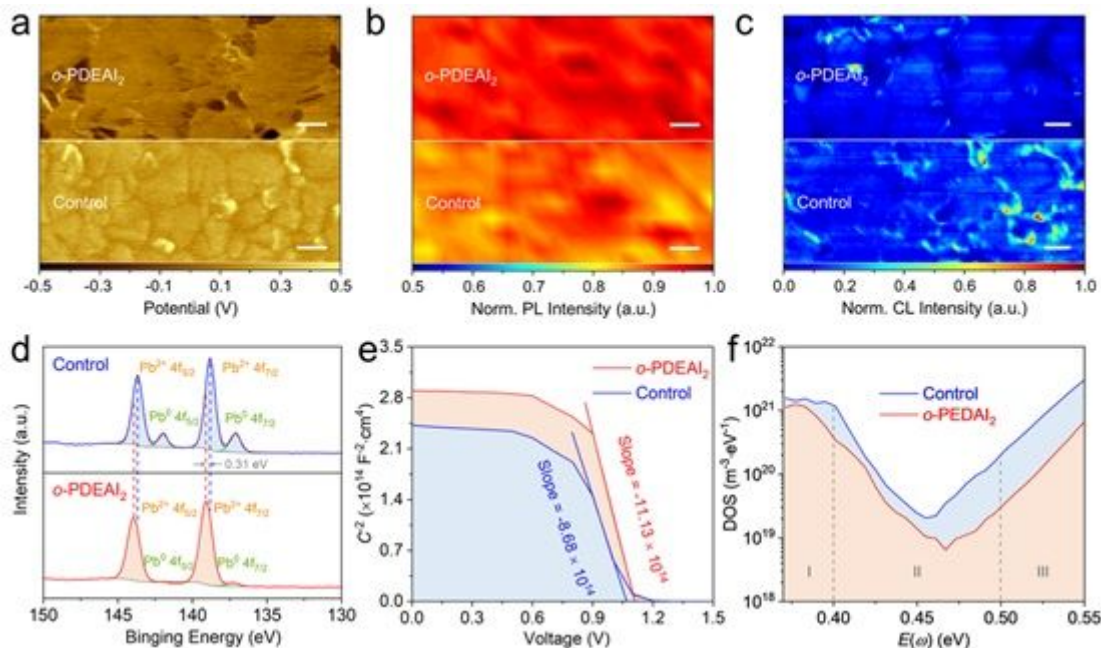

Figure 4

Characterization of the perovskite films and interface with o-PDEAl2. a, KPFM images of perovskite films showing the electronic chemical potential. b, Normalized PL intensity maps of the perovskite films illustrating the film homogeneity. c, Normalized CL mapping images of the perovskite films. d, High-resolution Pb 4f core-level XPS spectra of perovskite films. e, Mott-Schottky plots of the devices revealing the interfacial charge density. f, tDOS distribution in PSCs showing less trap densities after o-PDEAl2 passivation.
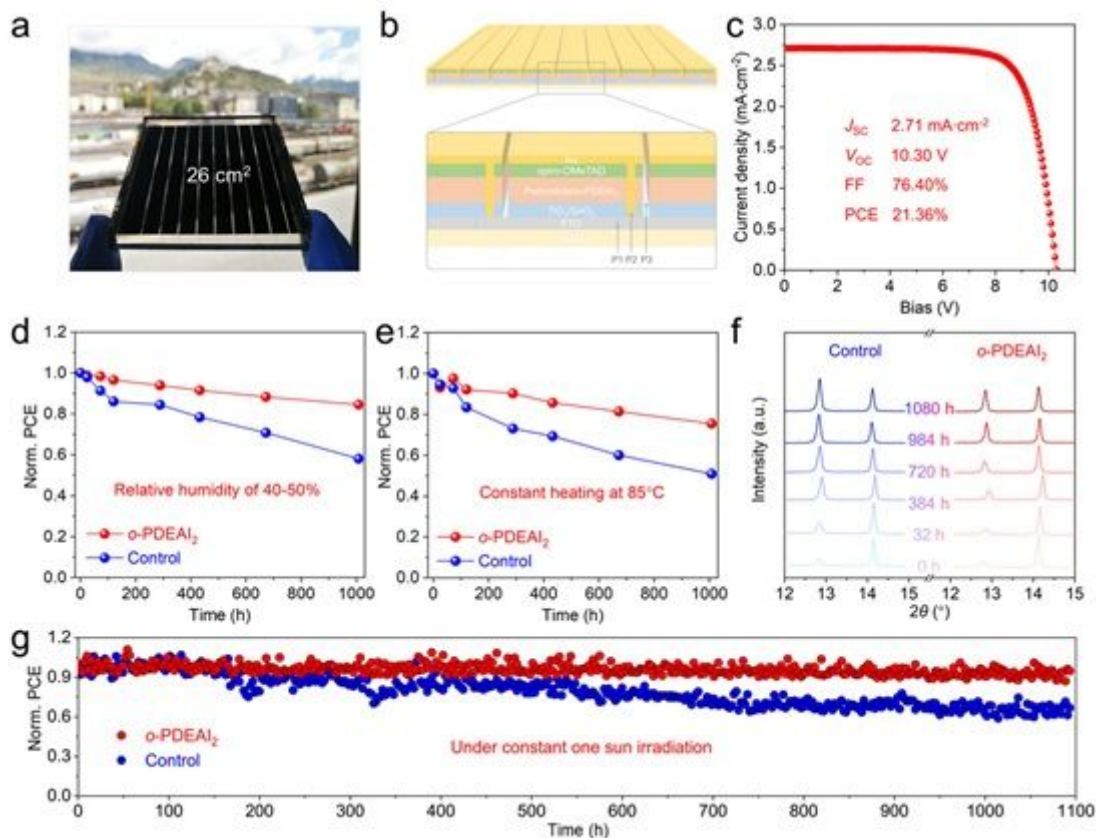
Figure 5

Module performance and long-term stability of the PSCs. a, Photograph of the fabricated perovskite solar module. b, Schematic showing the interconnections of the module. c, J-V characteristics of the champion perovskite solar module with an active area of 26.00 cm2. d, Evolution of the PCEs for the unencapsulated devices exposed to a controlled relative humidity (RH) of 40%-50% in the dark. e, Evolution of the PCEs for the unencapsulated devices under constant heating at 85°C in a nitrogen atmosphere. f, XRD patterns of the perovskite films as a function of annealing time at constant 85°C. g, Maximum power point tracking (MPPT) for 1100 hours of the unencapsulated devices under continuous light (100 mW cm-2) illumination at 25°C in a nitrogen atmosphere.

Supplementary Files

This is a list of supplementary files associated with this preprint. Click to download.

- Supplementaryinformation20072021.docx